

Selected Papers

Two-Dimensional Melting and Phase Change of Binary Mixtures of CCl_4 and $CHCl_3$ Confined in ACF Nanospace Studied Using Solid-State ^1H NMR

Takahiro Ueda,*[1,2,†] Hiroaki Omichi,[1] Yu Chen,[1] Hirokazu Kobayashi,[1] Osamu Kubota,[1] Keisuke Miyakubo,[1] and Taro Eguchi[1,2]

[1]Department of Chemistry, Graduate School of Science, Osaka University, Toyonaka, Osaka 560-0043

[2]The Museum of Osaka University, Osaka University, Toyonaka, Osaka 560-0043

Received June 28, 2010; E-mail: t_ueda@toyo.jp

Two-dimensional melting and phase changes of binary mixtures of CCl_4 and $CHCl_3$ confined in activated carbon fiber were examined using differential thermal analysis and ^1H wide-line NMR. Molecular assembly of CCl_4 confined in ACF nanospace with a slit width of 1.1 nm showed succeeding thermal anomalies corresponding to crystal–hexatic and hexatic–liquid transitions. Results showed that these thermal anomalies did not occur in a mixture of $CHCl_3$ and CCl_4. This behavior differed greatly from the phase diagram for the bulk mixture between $CHCl_3$ and CCl_4. Furthermore, the dynamic features of $CHCl_3$ molecule were examined using the ^1H wide-line NMR spectrum. The activation energy of the hopping motion changed from 7 kJ mol^{-1} for pure $CHCl_3$ to 13 kJ mol^{-1} for $CHCl_3$ with a 0.016 molar ratio in CCl_4. In particular, a drastic increase in the activation energy was observed for doping with a trace amount of $CHCl_3$, suggesting that molecular self-assembly of CCl_4 takes place in the ACF nanoslit because of the effective intermolecular interaction between CCl_4 molecules. The existence of $CHCl_3$ in CCl_4 brings about the remarkable impurity effect on two-dimensional melting and phase transition of CCl_4 confined in ACF nanospace.

Geometrical restriction of molecular assembly causes specific characteristics that differ from that of bulk material. Nanometer-sized free space, so-called "nanospace," provides a typical and ideal field of geometrical restriction for many molecular assemblies. In such spaces, enhancement of intermolecular interaction between admolecules and pore walls perturbs the intermolecular interactions of the guest molecules effectively. This situation affects the Gibbs energy of the molecular assembly of guests thermodynamically through surface energy between the pore-walls and the guest molecules.[1–3] In this context, thermodynamic properties such as melting/freezing and phase transition temperatures differ from those in the bulk.[4] This behavior has been described using the Gibbs–Thomson equation as the surface energy effect. According to this equation, although the surface effect brings depression of melting points in many cases,[5–8] some guest molecules exhibit elevation of the melting point in nanospace by the effect of guest–wall interactions, which cause the surface tension of the liquid state to be greater than that of the solid state.[9,10]

Carbon tetrachloride (CCl_4) confined in an activated carbon fiber (ACF) is one example of melting point elevation. Radhakrishnan et al. investigated the melting of CCl_4 confined in ACFs using DSC measurements. Their results showed that interaction between CCl_4 and nanographites raises the melting point of CCl_4 in ACF nanopores about 50 K compared to bulk liquid.[9] The ACF consists of micrographites of about 2 nm × 2 nm, and forms a slit nanospace as the interstices of micrographite stacking.[11–13] The hydrophobicity of ACF pore walls effectively attracts CCl_4. Taking account of the effective hydrophobic interaction between ACF and CCl_4, Grand canonical Monte Carlo (GCMC) simulation reproduced the elevation of the melting point of CCl_4 in ACF.[10]

In addition, the ACF nanoslit provides a quasi-two-dimensional (2D) potential field in the nanospace. The decrease in the dimensionality of space also affects the intermolecular interaction of the confined guest molecules, giving rise to their specific behaviors as a 2D fluid. Especially, melting and phase change phenomena have attracted much attention for their role in elucidating a topological phase transition in a 2D fluid.[14–16] According to the Kosterlitz–Thouless–Halperin–Nelson–Young (KTHNY) theory,[17–20] 2D crystal melts via an intermediate phase—a so-called "hexatic phase"—similarly to smectic B liquid crystal. Crystal–hexatic transition takes place by dissociation of dislocation pairs. Then a hexatic–liquid transition occurs by dissociation of disclination pairs from a statistical mechanics viewpoint.[17] In fact, the nonlinear dielectric effect shows the crystal–hexatic transition of the CCl_4 globular

† Present address: Department of Applied Chemistry, Faculty of Science and Engineering, Toyo University, 2100 Kujirai, Kawagoe, Saitama 350-8585

Published on the web October 30, 2010; doi:10.1246/bcsj.20100169

molecule in the ACF quasi-2D nanopores, as well as the hexatic–liquid transition.[21] In the hexatic phase, CCl_4 molecules form a 2D layered structure in which each molecule is arranged locally in a pseudo-hexagonal lattice, but not with long-range order among molecules. Consequently, the intermolecular interaction in the anisotropic space makes it possible to provide a specific and particular local structure and dynamics of guest molecules.

To elucidate the phase transition mechanism in a 2D fluid, it is necessary to know the dynamic fluctuation of the local structure of guest molecules. Iiyama and co-workers investigated the local structure of CCl_4 in ACF using XRD, SAXS, and GCMS.[22–25] They found that ACFs accommodate CCl_4 homogeneously in the nanoslit and that the organized CCl_4 assemblies are limited to within the fourth-neighbor coordination. Furthermore, GCMS predicted the bilayer structure of CCl_4 assemblies in the slit separation of 1–1.3 nm. Especially, CCl_4 molecular assemblies form organized and regular molecular arrangement like a thin three-dimensional bulk crystal when the slit width is 1 nm. However, dynamic aspects of CCl_4 in ACF have not yet been clarified. Recently, we conducted ^{2}H NMR and DTA studies of $CHCl_3$ confined in ACF.[26] A thermal anomaly of $CHCl_3$ in ACF was found at a different temperature from that of bulk of $CHCl_3$. Based on the molecular motion of $CHCl_3$ in ACF, we discussed the possibility of crystal–hexatic or hexatic–liquid phase transitions of $CHCl_3$ in ACF. Consequently, a trace amount of $CHCl_3$ in CCl_4 is expected to be a good probe for monitoring the molecular motion of CCl_4 in ACF. Furthermore, the rotational diameter of 0.54 nm in $CHCl_3$ is about 8.5% less than 0.59 nm for CCl_4, and the polarizability of 8.23×10^{-30} m^3 for $CHCl_3$ is less than 10.5×10^{-30} m^3 for CCl_4. These features are also expected to give effective perturbation of the intermolecular interaction between CCl_4 molecules in ACF from the reduction of both molecular size and dispersion force: in CCl_4/$CHCl_3$ binary systems, the $CHCl_3$ concentration dependence of phase behavior as well as molecular motion will provide a new and remarkable insight into understanding of the phase transition mechanism.

In this study, we examined a mixture of CCl_4 and $CHCl_3$ coadsorbed in the ACF slit nanospace. Use of $CHCl_3$ makes it possible to detect an ^{1}H NMR signal as a probe molecule. Then we discussed the molecular motion and intermolecular interaction of CCl_4 in ACF through the molecular motion of $CHCl_3$. We first examined thermal properties of CCl_4, $CHCl_3$, and their mixtures confined in ACF. The thermal properties have been discussed based on the phase diagram of bulk mixtures of CCl_4 and $CHCl_3$. The molecular motion of $CHCl_3$ in the mixture of CCl_4 and $CHCl_3$ confined in ACF has also been examined using ^{1}H NMR. Finally, we described the intermolecular interaction and the local structure of adsorbates in the ACF nanopore; then we discussed the mechanism of hexatic phase formation of CCl_4 and the effect of $CHCl_3$ doping in CCl_4 on the transition behavior.

Experimental

Sample Preparation. Pitch-based activated carbon fiber (ACF-A20; Osaka Gas Co., Ltd.) specimens were used. They were characterized using the N_2 adsorption isotherm at 77 K. Details of those analyses have been reported elsewhere.[27] The micropore volume (W_0) and the slit pore width (w) were, respectively, $0.90 \pm 0.02 \times 10^{-6}$ m^3 g^{-1} and 1.1 ± 0.1 nm.

The saturated amount of adsorbate was determined by monitoring the weight gain of the sample. The fibrous ACF-A20 sample was evacuated at 473 K for 2 h in vacuum following evacuation at room temperature for 1 day. The pretreated sample was put into a glass bottle of 5 mmϕ, which was then put inside a larger one (12 mmϕ with a sealing cap) to expose ACF to adsorbate vapor ($CHCl_3$ or CCl_4) at room temperature. The ACF sample was kept under the adsorbate vapor. Then sample was weighed in an appropriate time interval to monitor the weight gain. At 3 h after exposure to $CHCl_3$ vapor, the sample weight became constant at 1.22 ± 0.07 g/1 g ACF. The same procedure gives 1.43 g/1 g ACF for the saturated amount of CCl_4 in ACF. Dividing these amounts by the pore volume gives the effective density of adsorbate in ACF: 1.36 g cm^{-3} for $CHCl_3$ and 1.59 g cm^{-3} for CCl_4. The effective density of $CHCl_3$ in ACF is somewhat less than 1.479 g cm^{-3} at 298 K in the bulk liquid $CHCl_3$, although it is comparable to 1.594 g cm^{-3} at 298 K in bulk liquid of CCl_4. These effective densities also provide the spatial occupation of adsorbate to the ACF nanospace: 56% for $CHCl_3$ and 67% for CCl_4 (vide infra).

Samples for the NMR measurement were prepared according to the following procedures: The powdered ACF-A20 samples were evacuated at 473 K for 2 h after evacuation at room temperature for 1 day under reduced pressure ($<1.3 \times 10^{-3}$ kPa). The pre-treated powders were exposed to the vapor of adsorbate at room temperature for 2 days using a vacuum line. The prepared specimens were sealed into glass ampoules (5 mmϕ) with He gas (35 kPa). The adsorbates, $CHCl_3$ (99.8%) and CCl_4 (99.8%) (Wako Pure Chemical Industries, Ltd.) were used in preparation without further purification. The fraction of $CHCl_3$ in the mixed vapor was evaluated from $CHCl_3$–CCl_4 vapor–liquid equilibrium data: $f(CHCl_3) = 0.016$, 0.16, and 0.63. Assuming that the selective adsorption of each vapor to ACF was negligible, we approximately regarded the molar fraction of $CHCl_3$ in bulk vapor as that in ACF, because it was difficult to determine the exact concentration of each substance in adsorbate confined in ACF.

The samples for differential thermal analysis (DTA) measurements were prepared according to the following procedure: The pretreated ACF-A20 powders were put into a DTA sample tube. Then 1.1–1.5 times the pore volume of bulk liquids of $CHCl_3$, CCl_4, and/or mixtures of $CHCl_3$ and CCl_4 were added using a microsyringe. The resultant sample tubes were sealed off after loading N_2 gas (30–40 kPa). The sealed tubes remained static for 2 days until the adsorption equilibrium was achieved. In this case, the molar fraction of $CHCl_3$ in ACF was approximated by the molar fraction of $CHCl_3$ in the bulk mixed solution added to ACF. A bulk phase diagram of mixtures of $CHCl_3$ and CCl_4 was prepared using 12 mixtures with the following molar ratios: $f(CHCl_3) = 0.025$, 0.05, 0.1, 0.2, 0.3, 0.4, 0.5, 0.6, 0.7, 0.8, 0.9, and 0.95.

NMR Measurements. The ^{1}H NMR measurements were conducted using a spectrometer (DSX-200; Bruker Analytik GmbH) equipped with a superconducting magnet (4.7 T), operated at the Larmor frequency of 200.13 MHz for protons.

Free induction decay (FID) signals were recorded using a single-pulse experiment. The length for 90° pulse was 2.3–2.8 μs, and the pulse delay was 4 s. The ^{1}H chemical shift was referred using a signal from neat $CHCl_3$ at 7.27 ppm from TMS. Sample cooling was conducted by flowing evaporated N_2 gas. The temperature was controlled within experimental error of ±0.5 K using a temperature control unit (VT-3000; Bruker); spectra were observed at temperatures of 130–298 K.

DTA Measurements. Differential thermal analysis (DTA) was conducted using a custom-built apparatus at temperatures of 150–350 K. An α-Al_2O_3 powder was used as a reference. The DTA diagrams were recorded in both heating and cooling directions. The rate of temperature increase was about 1–1.5 K min^{-1}. Furthermore, the measurements were repeated several times to check the thermal hysteresis. For preparation of a phase diagram of bulk $CHCl_3$–CCl_4 binary mixtures, DTA diagrams were measured only on heating and the temperature of the endothermic peaks was plotted against the molar fraction of CCl_4.

Results and Discussion

Differential Thermal Analysis (DTA) of $CHCl_3$ and CCl_4 Confined in ACF. Figures 1a–1f show differential thermal analysis (DTA) diagrams for guest-free and guest-loaded ACFs greater than 260 K. Each curve was measured on heating. No peaks are apparent in guest-free ACF (Figure 1a), although two peaks are visible at 313 and 344 K in CCl_4-loaded ACF (Figure 1f). According to Cheung's model,[28] the slit width in this study (1.1 nm) is expected to yield a double minimum potential profile for CCl_4, which will engender the bilayer of CCl_4 in ACF (vide infra). Radhakrishnan et al. predicted that bilayered CCl_4 molecular assembly exhibits first-order phase transition.[21] In Figure 1f, the peak at 313 K swells from around 303 K and continues to ca. 320 K. If the starting temperature of this peak is used as a transition temperature, it agrees with the crystal–hexatic transition temperature, as detected using DSC (298 K), dielectric relaxation spectroscopy (DRS), and nonlinear dielectric effect (NDE) (295 K) for ACF.[21] In addition, the peak at 344 K is also distributed from 330 to 350 K. Since the baseline of the DTA diagram is curved largely, it is difficult to determine the temperature at which the peak stands up. However, seeing it carefully, it is found that the slope of the DTA diagram changes around 332 K. In this work, this temperature is regarded as the transition point. A thermal anomaly takes place in the same temperature region of the hexatic–liquid transition, which was reported by Radhakrishnan et al. Therefore, it will correspond to the hexatic–liquid transition, although the reported values (353 K from DSC and DRS, and 352 K from NDE)[21] are somewhat higher than the temperature observed in the present study. One of the possibilities for elevation of melting point may be difference in the pore size. In Ref. 21, the pore width is signified by H, which is the distance separating the planes through the centers of the carbon atoms in the first layer of the opposing walls. This representation is related to the empirical pore width (w) by the simple approximation, $w = H - \sigma_{ss}$ where σ_{ss} is Lennard–Jones σ parameter for the carbon atom–carbon atom interaction ($\sigma_{ss} =$ 0.34 nm). The ACF sample in Ref. 21 has the pore width of 1.4 nm as H, which corresponds to 1.06 nm as w. This pore width is close to 1.1 nm in our specimen. Therefore, the pore size will not affect the transition temperature effectively. The difference in the transition temperature may stem from the different conditions in the analytical, preparation and measurement methods, but it is difficult to identify the origin of the differences because of the complex system for CCl_4 adsorbed into ACF nanospace.

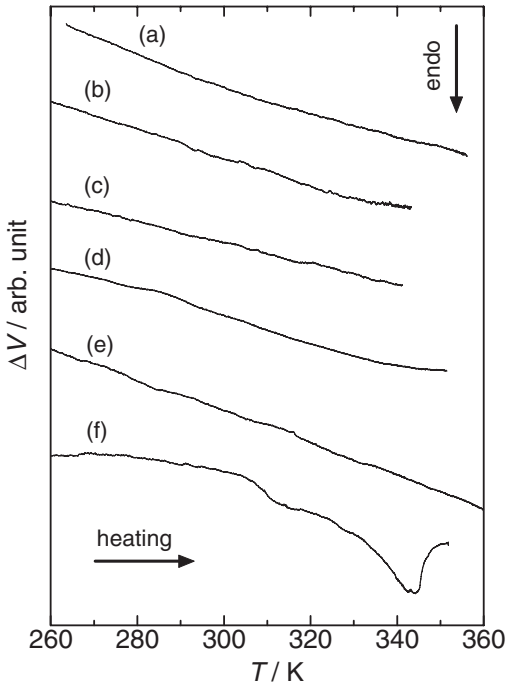

Figure 1. Differential thermal analysis (DTA) diagrams of guest-free ACF (a), ACF saturated with $CHCl_3$ (b), ACF saturated with CCl_4–$CHCl_3$ mixed vapor: $f(CHCl_3) = 0.5$ (c), 0.1 (d), 0.024 (e), and ACF saturated with CCl_4 (f).

Consequently, this supports the findings of the hexatic phase of CCl_4 in ACF reported by Radhakrishnan et al.[21] CCl_4 molecules confined in ACF are regarded as a 2D crystal and/or fluid, and the melting and/or freezing will obey the KTHNY theory. On the other hand, $CHCl_3$-loaded ACF shows no thermal anomaly from 260 to 350 K in the same DTA scale (Figure 1b), although a small peak detectable with the more sensitive DTA scale is distributed from 250 to 287 K.[26]

Bulk $CHCl_3$ and CCl_4 melt at 209.5 and 250 K, respectively. In addition, CCl_4 has a plastic phase in the temperature range from 225.5 K to melting point. In contrast, mixtures of each bulk material engender the impurity effect of each other, and melting points are expected to be depressed. However, a solid–liquid phase diagram of a bulk CCl_4–$CHCl_3$ binary system has not been reported as far as we know. In this work, we report the first solid–liquid phase diagram of a bulk CCl_4–$CHCl_3$ binary system. Figure 2 shows a phase diagram of a bulk CCl_4–$CHCl_3$ binary system, which was prepared from the temperature of endothermic peak observed on heating.

Results showed that these substances form a eutectic mixture in bulk. The phase diagram suggests that the eutectic point is 193 K at the composition of 40% CCl_4 and 60% $CHCl_3$. In compositions including a CCl_4 molar fraction of less than 40%, the solid–liquid equilibrium at temperatures greater than 193 K

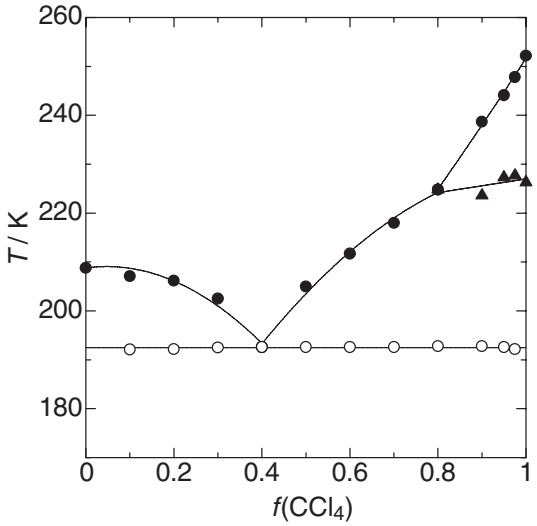

Figure 2. Phase diagram of CCl_4–$CHCl_3$ binary system prepared using DTA measurements. For preparation of phase diagram, all the measurements were conducted on the heating direction. The clear endothermic peaks were observed for melting of eutectic mixture, solid–solid transition, and melting of bulk pure compounds. The transition point was determined from the temperature at which the extrapolation of the slope at the low-temperature side for the endothermic peak crosses the baseline: Melting temperature of the eutectic mixture is represented by open-circle (○) and solid–solid phase transition temperature is represented by filled-triangle (▲). In contrast, for dissolution of pure $CHCl_3$ or CCl_4 solid into the solution of the melted eutectic mixture, the end point of the broad endothermic peak is regarded as the temperature at which dissolution was completed, and is represented by filled-circle (●). Melting point of bulk pure $CHCl_3$ ($f(CCl_4) = 0$) and CCl_4 ($f(CCl_4) = 1$) is also represented by filled-circle (●).

obeys a liquidus curve of bulk $CHCl_3$. In this region, the solid phase of bulk $CHCl_3$ coexists with liquid phase of bulk $CHCl_3$–CCl_4 mixture. On the other hand, in compositions including a CCl_4 molar fraction of more than 40%, the solid–liquid equilibrium at temperatures greater than 193 K obeys a liquidus curve of bulk CCl_4. In this region, the solid phase of pure bulk CCl_4 coexists with liquid phase of bulk $CHCl_3$–CCl_4 mixture. When the melting point lowers in comparison with the solid–solid transition point of bulk CCl_4, the CCl_4–$CHCl_3$ binary system shows no phase transition before melting. Above a 0.8 molar fraction of CCl_4, the melting point is higher than the transition point, and the plastic phase of CCl_4 appears even in the CCl_4–$CHCl_3$ binary system. Consequently, the CCl_4–$CHCl_3$ binary system shows a similar phase relation to that of pure bulk CCl_4 up to the composition of 80% CCl_4 and 20% $CHCl_3$.

In contrast, for a CCl_4–$CHCl_3$ binary system confined in ACF, we found that the phase transitions of CCl_4 in ACF disappear when $CHCl_3$ is admitted into CCl_4. The ACF accommodating mixture of CCl_4 and $CHCl_3$ shows no peak at temperatures of 260–340 K. Even in CCl_4 with only a 2.4% molar fraction of $CHCl_3$, neither endothermic peak corresponding to a crystal–hexatic or hexatic–liquid transition is visible (Figure 1e). The effect of the $CHCl_3$ addition on the thermodynamic properties in a 2D system is more responsive than that in a bulk system. In general, addition of impurity into a homogeneous system increases the system's entropy: a small amount of $CHCl_3$ destroys the structural coherency between the CCl_4 molecules in ACF, resulting in decrease of the hexatic bond-orientational order in 2D CCl_4 crystal. This will also engender the dynamic disorder of the CCl_4 molecules in the adsorbed structure. In the following section, we will describe the effect of addition of $CHCl_3$ on the molecular motion of CCl_4 in ACF.

^{1}H NMR of $CHCl_3$ Coexisting with CCl_4 in ACF. To examine the effect of $CHCl_3$ on the local structure and dynamic behavior of CCl_4 in ACF nanoslits, the temperature dependence of the ^{1}H NMR spectrum for $CHCl_3$ was measured on ACF accommodating $CHCl_3$–CCl_4 mixed solution with the molar fraction of $CHCl_3$ or pure $CHCl_3$: $f(CHCl_3) = 0.016$, 0.16, 0.63, and 1. The observed spectra are presented in Figure 3. Each specimen gives a single narrow peak with FWHM less than 1 kHz at ambient temperature. For $f(CHCl_3) = 0.16$, 0.63, and 1, the peak shifts more than 10 ppm toward higher frequency when temperature decreases. The large temperature dependence of the chemical shift is caused by the pseudo-contact interaction with paramagnetic spins in graphenes, because the ^{1}H chemical shift is normally distributed over only 10 ppm in the diamagnetic compounds. In contrast, the specimen with $f(CHCl_3) = 0.016$ shows the temperature dependence of the chemical shift different from other specimens; the peak shows low frequency shift from 298 to 260 K and then shifts to high frequency like other specimens. As described below, $CHCl_3$ in ACF with $f(CHCl_3) = 0.016$ interacts with the surrounding CCl_4 effectively, and undergoes very slow motion in comparison with other specimens. The origin of the low frequency shift is not clear, but it is probably related to motion such as the slow chemical exchange between the adsorption sites.

On the other hand, the line width broadens with decreasing temperature, implying that the molecular motion of $CHCl_3$ slows when temperature decreases. Almost all the spectra are reproducible with a Lorentzian line shape, whereas in the low molar fraction of $CHCl_3$ less than 0.16 the spectra obtained at low temperatures are reproducible by superposition of two Lorentzian functions. The major and narrow component originates from $CHCl_3$ confined in ACF, but the minor and broader component ($\Delta\nu_{1/2} > 10$ kHz) is expected to be protons bonded to aromatic and/or aliphatic carbons at the edges of micrographenes in ACF. The resultant FWHMs ($\Delta\nu_{1/2}$) for $CHCl_3$ are shown against temperature in Figure 4.

In the specimen with $f(CHCl_3) = 0.016$, line broadening begins at less than 260 K and rises up to ca. 6 kHz less than 150 K. As the molar fraction of $CHCl_3$ increases, the temperature at which the broadening begins becomes lower, and the observable maximum line width narrows. When $f(CHCl_3) = 1$, the line broadening appears at less than 150 K, and only just rises up to ca. 2 kHz at 120 K. These aspects suggest that the mobility of $CHCl_3$ depends strongly on the molar fraction of $CHCl_3$, and that admission of $CHCl_3$ facilitates molecular motion. Because the ^{1}H NMR line width is responsive to the

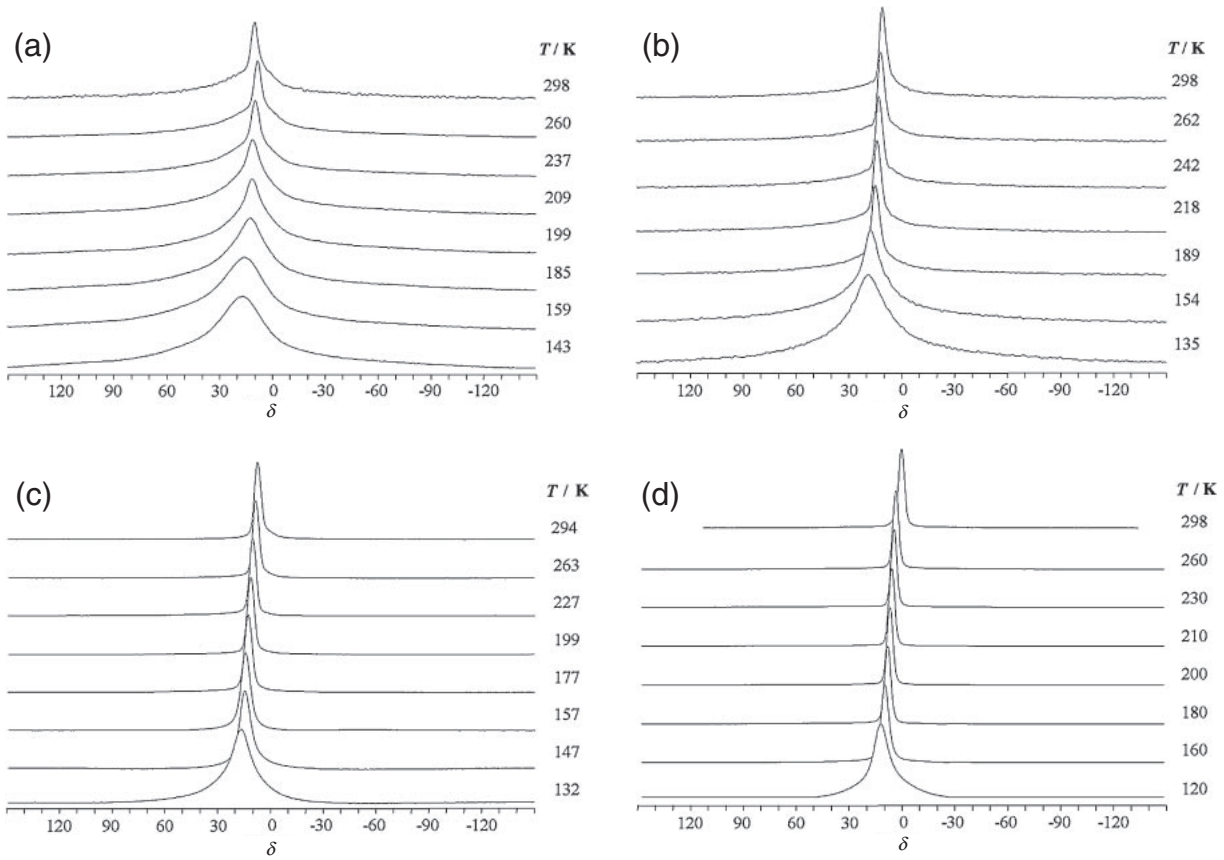

Figure 3. Temperature dependence of ^{1}H NMR spectrum for $CHCl_3$ in ACF accommodating $CHCl_3/CCl_4$ mixed solution with the molar fraction of $CHCl_3$: $f(CHCl_3) = 0.016$ (a), 0.16 (b), 0.63 (c), and pure $CHCl_3$ (d).

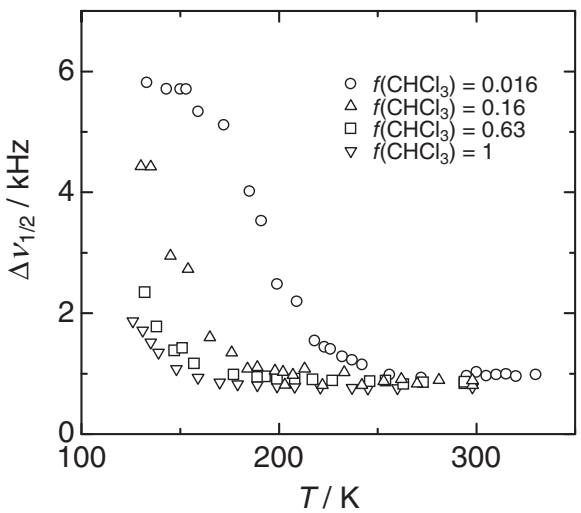

Figure 4. Temperature dependence of full line width at half maximum ($\Delta\nu_{1/2}$) in a ^{1}H NMR spectrum. Almost all the spectra are reproducible with a single Lorentzian function, whereas in the low molar fraction of $CHCl_3$ the spectra obtained at low temperatures are reproducible by superposition of two Lorentzian functions. In the latter case, one component originates from $CHCl_3$ confined in ACF. The other one ($\Delta\nu_{1/2} > 10$ kHz) is expected to be protons bonded to aromatic and/or aliphatic carbons at the edges of micrographenes in ACF. Only the contribution of $CHCl_3$ is shown as $\Delta\nu_{1/2}$ values in the figure.

molecular motion in a frequency range similar to the line width, $CHCl_3$ molecules are expected to undergo molecular motion at frequencies of 1000 Hz and higher, but not at frequencies higher than the Larmor frequency (2×10^8 Hz). This slow motion is on a time scale of the translation or chemical exchange between the stable adsorption sites, rather than the molecular reorientation.

We can evaluate the correlation time of $CHCl_3$ from the temperature dependence of the ^{1}H NMR line width using the following equation:[29]

$$(\Delta\nu_{1/2})^2 = M_2'' + M_2'(2/\pi)\tan^{-1}(2\pi \cdot \alpha \cdot \Delta\nu_{1/2} \cdot \tau_c) \quad (1)$$

where M_2'' and M_2' respectively signify the second moment of the resonance line for the residual line width and for the rigid lattice, and α stands for a numerical factor of order unity ($\alpha \approx 5$ in our analysis). In this study, the spectra are almost approximated by Lorenztian line shape, for which it is difficult to represent the second moment of resonance line using the line width, because the estimation of the second moment depends strongly on the truncation of decay of the resonance line. However, the second moment is in the same order of the square of the line width of the resonance line. Therefore, the M_2'' and M_2' were simply approximated by the square of the residual line width after motional narrowing and the square of the broadened line width, respectively. For the M_2' value, the line width broadened up to 5.8 kHz in the sample with $f(CHCl_3) = 0.016$. In this case, the contribution of the intermolecular ^{1}H–

^{1}H dipolar interaction of $CHCl_3$ to the line width is negligible because of the extremely low molar fraction of $CHCl_3$. The dipolar interaction between ^{1}H and electron spins in the ACF framework and/or the inhomogeneity of the volume susceptibility will be mainly attributable to this broadening. In addition to this broadening, the intermolecular ^{1}H–^{1}H dipolar interaction among $CHCl_3$ molecules contributes to the line width in specimens with more $CHCl_3$. The isotropically rotating $CHCl_3$ molecule is regarded as a sphere of 0.54 nm diameter. In this case, the intermolecular ^{1}H–^{1}H dipolar interaction can be approximated very well by counting the ^{1}H–^{1}H vectors between protons located at the center of gravity.[30] Assuming the close-packing and the bilayer formation of $CHCl_3$ in ACF, and taking account of the contribution of the nine nearest neighbors, a proton at the center of a sphere mainly interacts with the protons locating at the center of the surrounding spheres. The intermolecular ^{1}H–^{1}H dipolar interaction from the nearest neighbors gives rise to the line broadening. The expected second moment M_2 of the ^{1}H resonance line can be estimated as $2.3 \times 10^6\,\mathrm{Hz}^2$ for the specimen with $f(\mathrm{CHCl_3}) = 1$ using the following relation:[31]

$$M_2 = \frac{3}{5}\gamma^4\hbar^2 I(I+1)\cdot f(\mathrm{CHCl_3})\cdot N\cdot\frac{1}{r^6} \qquad (2)$$

where γ signifies the ^{1}H gyromagnetic ratio, I denotes the nuclear spin ($I = 1/2$ for proton), r stands for the internuclear distance between protons, and N is the number of spins for nearest neighbors. The estimated M_2 value corresponds to the 3.6 kHz full width at half maximum for the Gaussian line shape through the following relation: $\Delta\nu_{1/2} = 2.36\sqrt{M_2}$. In two other specimens, the intermolecular ^{1}H–^{1}H dipolar interaction is reduced by the molar fraction of $CHCl_3$: the expected second moments for the specimens with $f(\mathrm{CHCl_3}) = 0.16$ and 0.63 are 3.7×10^5 and $1.5 \times 10^6\,\mathrm{Hz}^2$, respectively, which gives the line width corresponding to 1.5 and 2.9 kHz. These additional dipolar interactions contribute to intrinsic line broadening between $CHCl_3$ and the ACF nanoslit. Therefore, the M_2' value can be approximated by the sum of the square of the intrinsic line width (5.8 kHz) and the estimated line width for intermolecular ^{1}H–^{1}H dipolar interaction, and it then is expected to yield the corresponding M_2' value of 3.4×10^7 Hz^2 for $f(\mathrm{CHCl_3}) = 0.016$, $3.6 \times 10^7\,\mathrm{Hz}^2$ for $f(\mathrm{CHCl_3}) = 0.16$, $4.2 \times 10^7\,\mathrm{Hz}^2$ for $f(\mathrm{CHCl_3}) = 0.63$, and $4.7 \times 10^7\,\mathrm{Hz}^2$ for $f(\mathrm{CHCl_3}) = 1$. Figure 5 shows that the assumptions on M_2'' and M_2' enable us to evaluate the correlation time (τ_c) from the experimental $\Delta\nu_{1/2}$ values. The τ_c value distributes from 10^{-8} to 10^{-4} s, and the temperature dependence of τ_c obeys Arrhenius' law in all samples. The time region in which these τ_c values are much longer than the τ_c value (10^{-11}–10^{-10} s) for the rotational diffusion is determined from ^{2}H T_1, and is consistent with time scale of molecular motion engendering the motional narrowing of spectrum effectively (10^3–10^8 Hz).[26] Therefore, the detectable dynamic process by ^{1}H line broadening is expected to be much slower than the rotational diffusion, and is expected to reflect the local motion of $CHCl_3$ in ACF, as in a chemical exchange between the adjacent adsorption sites. This picture is consistent with molecular motion of $CDCl_3$ in ACF.[26] The τ_c value becomes longer with increased molar fraction of CCl_4: the existence of CCl_4 enhances structural ordering of the guest molecules in ACF, and slows the mobility of $CHCl_3$. This also reflects the activation energy that is evaluated from the slope in Figure 5. The E_a value for $CHCl_3$ in the mixture of CCl_4 and $CHCl_3$ confined in ACF depends on the molar fraction of $CHCl_3$. Figure 6 shows the dependence of E_a on the molar fraction of $CHCl_3$. The E_a value for $f(\mathrm{CHCl_3}) = 1$ agrees well with that evaluated from ^{2}H T_2* less than 227 K (7.7 kJ mol^{-1}).[26] When the molar fraction of $CHCl_3$ decreases (increase in the molar fraction of CCl_4) from 1 to 0.2, the E_a value increases gradually and linearly with $f(\mathrm{CHCl_3})$, but a remarkable increase in the E_a value is observed for $f(\mathrm{CHCl_3}) = 0.016$ and the E_a value reaches 13 kJ mol^{-1}.

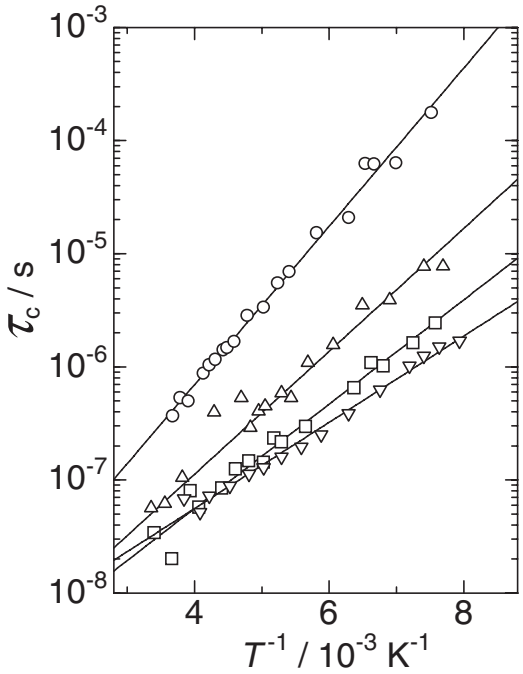

Figure 5. Arrhenius plot of correlation time (τ_c) for molecular hopping of $CHCl_3$ in ACF accommodating $CHCl_3/CCl_4$ mixed solution with the molar fraction of $CHCl_3$: $f(\mathrm{CHCl_3}) = 0.016$ (○), 0.16 (△), 0.63 (□), and pure $CHCl_3$ (▽).

This aspect provides us the local structure of $CHCl_3$ in the binary mixture of CCl_4 and $CHCl_3$ under the conditions confined into the ACF nanoslit, because the E_a value of a $CHCl_3$ molecule is influenced by the intermolecular interaction between the nearest-neighboring molecules at the first approximation. Assuming that both CCl_4 and $CHCl_3$ are homogeneously mixed in ACF and the number of the nearest neighbors around a $CHCl_3$ molecule is invariant over all mixing ratios, the population of CCl_4 in the nearest-neighboring molecules will linearly increase when $f(\mathrm{CHCl_3})$ decreases. This situation is consistent with the dependence of E_a on $f(\mathrm{CHCl_3})$. That is, in the mixture with $f(\mathrm{CHCl_3})$ from 1 to 0.2, both CCl_4 and $CHCl_3$ are mixed homogeneously, and additivity of the intermolecular interaction is achieved. As a result, it was found that the $CHCl_3$–CCl_4 interaction stabilized the site energy of $CHCl_3$ molecules more effectively than $CHCl_3$–$CHCl_3$ interaction. In contrast, the E_a value is clearly displaced from the linear

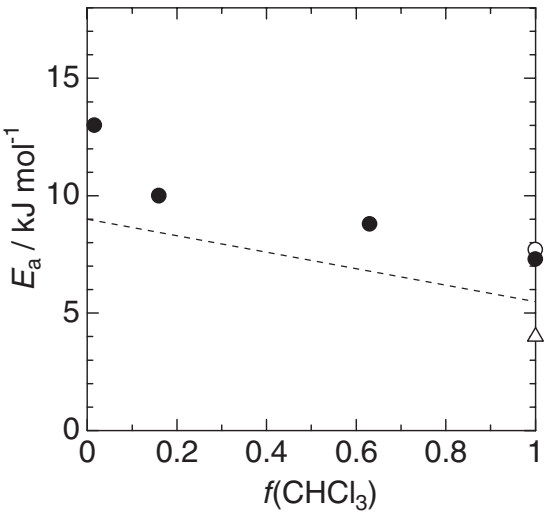

Figure 6. Dependence of the activation energy for molecular hopping of $CHCl_3$ on the molar fraction of $CHCl_3$ in $CHCl_3/CCl_4$ mixture. The white circle and triangle show the activation energy of $CDCl_3$ in ACF, as determined by temperature dependence of ^2H NMR line width (see Ref. 26). The dashed line shows the activation energy expected by the dispersion force between guest molecules when $CHCl_3$ and CCl_4 molecules are statistically distributed against the molar fraction of $CHCl_3$.

dependence on $f(CHCl_3)$ in the mixture with $f(CHCl_3) = 0.016$. In this molar fraction, a probe molecule, $CHCl_3$, is isolated from other $CHCl_3$ molecules and is surrounded by only the CCl_4 nearest neighbors. The sudden increase in the E_a value suggests the effective stability of the site energy in CCl_4 confined in ACF.

Consequently, τ_c and E_a for $CHCl_3$ in $CHCl_3$–CCl_4 mixed solution adsorbed into the ACF nanoslits reveal that the mobility of the CCl_4 molecules is lower than that of $CHCl_3$. This feature implies that the CCl_4 molecules are likely to form an ordered structure such as the hexatic phase in the ACF nanoslits.

Local Structure of $CHCl_3$ and CCl_4 in ACF Nanospace. In ACF slit pores, the potential profile dominating the expected equilibrium position of the guest molecules is given by the overlapping of the potentials acting between the guest and walls. According to Cheung, the potential profile between the guest molecule and pore walls is represented using the 12–6 Lenard–Jones potential when a rigid globular guest molecule is in the space of infinite parallel carbon sheets:[27,28,32]

$$U(y) = -\left(\frac{2\pi\varepsilon_{G\text{–}C}n}{5}\right)\left[\frac{5(R/2a_{G\text{–}C} - y/a_{G\text{–}C})^6 - 2}{(R/2a_{G\text{–}C} - y/a_{G\text{–}C})^{10}} + \frac{5(R/2a_{G\text{–}C} + y/a_{G\text{–}C})^6 - 2}{(R/2a_{G\text{–}C} + y/a_{G\text{–}C})^{10}}\right] \quad (3)$$

where $\varepsilon_{G\text{–}C}$ is the depth of the potential well, $a_{G\text{–}C}$ represents the average value of LJ a-parameter for G–C pair, R is the separation of pore walls, and the variable y is the distance between the guest molecule and pore wall ($-R/2 < y < R/2$). This potential function is not major, in comparison with other potential functions such as Steele's 10–4–3 potential.[33] However, Cheung's potential has an advantage that the type of the potential profile (single- or double-minimum shape) can be checked easily using the pore width and the diameter of the guest molecule. As we just need the shape of the potential profile for $CHCl_3$ and CCl_4 molecules in ACF, Cheung's potential is convenient for our purpose. Based on this equation, the shape of the potential profile depends critically on the ratio ($R/a_{G\text{–}C}$). This equation gives a double-minimum potential profile for $R/a > 2.4$ and a single-minimum potential profile for $R/a < 2.4$.[28,32] The diameter of the isotropically rotating molecule is 0.54 nm for $CHCl_3$ and 0.59 nm for CCl_4, and the van der Waals diameter of carbon atom in graphene is 0.34 nm. The a value is given by the average between the rotating diameter of guest molecule and the van der Waals diameter of carbon atom. Consequently, the R/a value is evaluated by the sum of the van der Waals radius of carbon atom and guest molecule, and is 2.5 for $CHCl_3$ and 2.56 for CCl_4. Each ratio suggests the double minimum potential profile and formation of the bilayer adsorption structure in ACF.

As described in the experimental section, the effective density of adsorbate in ACF is estimated to be 1.36 g cm^{-3} for $CHCl_3$ and 1.59 g cm^{-3} for CCl_4, based on the saturated amount of adsorption at room temperature. The effective density of $CHCl_3$ in ACF is somewhat less than 1.479 g cm^{-3} at 298 K in the bulk liquid, although it is comparable to 1.594 g cm^{-3} at 298 K in bulk liquid of CCl_4. In addition, assuming a rigid sphere for each guest molecule, the spatial occupancy of the guest molecules to the pore volume is roughly evaluated as 67% for CCl_4 and 56% for $CHCl_3$, using $(m_S \cdot N_A/M)(V_m/V_{pore})$ where m_S is the saturation amount of adsorption and V_m is the spherical volume of a rotating guest molecule. These values can be compared with the expected value of spatial occupancy, which is estimated as 65% for CCl_4 and 59% for $CHCl_3$ in 2D-slit with the slit width of 1.1 nm using the relation $(2\sqrt{3}/9)(d/w)$, when the rigid spheres occupy the ACF slit with ideal close-packing such as that of a crystal.

For CCl_4, the actual packing is somewhat dense in comparison with the expected one, implying that the close-packed and high-density structure of CCl_4 like a crystal is fulfilled in the ACF nanoslit. In fact, four nearest-neighbors form a tetrahedron in the bilayered close-pack structure of the rigid spherical molecules in the ACF nanoslit. For a 2D nanoslit with the slit width (w), the most effective packing will be achieved when the molecular diameter satisfies the relation: $3w/(3 + \sqrt{6})$. In the case of $w = 1.1$ nm, this relation engenders the preferable spherical diameter of approximately 0.6 nm. This diameter agrees well with that of CCl_4. That is, the ACF nanoslit with 1.1 nm slit width is preferred for CCl_4 to form the ideal close-pack structure. Consequently, the guest–wall as well as guest–guest interactions effectively stabilize the CCl_4 molecules in ACF. This situation will control the fluctuation of molecular arrangement, making it easy to form the structural ordering, and leading to the effective formation of "hexatic phase" of CCl_4 molecules because of the orientational bond ordering.

In contrast, for $CHCl_3$, the experimental value is somewhat less than the spatial occupancy for ideal close-pack of rigid spheres. Reduction of occupancy in $CHCl_3$ will occur because of the smaller molecular diameter than that of CCl_4. The molecular diameter of $CHCl_3$ corresponds to 90% of 0.6 nm,

which is the preferred molecular diameter for the ideal arrangement of guest molecules in the manner of bilayered close-pack structure. This situation engenders the large free space around a molecule and the loose stacking of the bilayer. It also facilitates the structural fluctuation of the $CHCl_3$ molecular assembly in ACF. Therefore, doping of $CHCl_3$ in CCl_4 assembly produces a free space around a $CHCl_3$ molecule because of the smaller molecular size and the weaker dispersion force of $CHCl_3$ than that of CCl_4. This effect reduces the structural order of the CCl_4 molecular assembly and enhances the molecular mobility of CCl_4. Consequently, it is considered that the orientational bond order will be reduced, and that the transition to hexatic phase then disappears.

Intermolecular Interaction of $CHCl_3$ and CCl_4 in ACF Nanospace. The activation processes detected by the temperature-dependent line width of ^{1}H NMR spectra are caused by the molecular jump between the nearest neighbor sites, as described above. In general, the formation of the vacancy available is known to require the largest energy barriers in the atomic or ionic hopping processes in a solid. Similarly, for the hopping process of the guest molecules in the 2D nanospace with the closed-packing of CCl_4 or $CHCl_3$, the formation of a vacancy must also give rise to the largest energy barrier, and correspond to the activation energy determined from the temperature dependence of the line width. Therefore, we will examine the intermolecular interaction with the surrounding nearest neighbors. Dispersion force mainly functions on CCl_4 because of nonpolar molecules, whereas dipole–dipole interaction also acts on $CHCl_3$ in addition to the dispersion force. Furthermore, in the mixture of CCl_4 and $CHCl_3$, the induced dipolar interaction will function between CCl_4 and $CHCl_3$.

The dispersion force (U_{dis}) is related to the polarizability (α) for interacting molecules. It is represented as $-(3/2)\alpha_1\alpha_2 I_1 I_2/[(4\pi\varepsilon_0)^2 r^6(I_1 + I_2)]$, where α_i and I_i respectively signify the polarizability volume and the ionization energy of molecule i, and r denotes the intermolecular distance.[34] The ionization energy for CCl_4 and $CHCl_3$ is approximately the same (ca. 11 eV), and the polarizability volume is 10.5×10^{-30} m^3 for CCl_4 and 8.23×10^{-30} m^3 for $CHCl_3$. Using these parameters, U_{dis} is evaluated as -2 kJ mol^{-1} for the CCl_4–CCl_4 pair, -1.5 kJ mol^{-1} for the CCl_4–$CHCl_3$ pair, and ca. -1.2 kJ mol^{-1} for $CHCl_3$–$CHCl_3$ pair for the intermolecular distance of 0.6 nm on the ideal close-packing structure in ACF with 1.1 nm slit width, as described above. The largest stability attributable to the intermolecular interaction is expected for CCl_4.

In contrast, the dipolar interaction (U_{dip}) between the isotropically rotating $CHCl_3$ molecules is presented as $-(2/3)\mu^2/[(4\pi\varepsilon_0)^2 r^6 kT]$, and the induced dipolar interaction (U_{ind}) between the rotating $CHCl_3$ molecule and CCl_4 molecule is given as $-\alpha\mu/[(4\pi\varepsilon_0)^2 r^6]$.[34] Using the dipolar moment (μ) of $CHCl_3$ (1.06 D), U_{dip} is evaluated as -26 J mol^{-1} for $CHCl_3$–$CHCl_3$ pair at room temperature and U_{ind} is -15 J mol^{-1} for the $CHCl_3$–CCl_4 pair. These are quite small in comparison with the dispersion force, and are negligible as the contribution of the intermolecular interaction to the guest molecules.

Regarding the close-packed bilayer structure of the guest molecules in the ACF nanoslit, a guest molecule has nine nearest neighbors: six neighbors in the same molecular layer and three neighbors in the other molecular layer. The dispersion forces mainly act between these molecules, as described above. A guest molecule feels the dispersion force of $U_{dis}/2$ because U_{dis} acts on a pair of molecules. Therefore, a molecule needs energy of $9U_{dis}/2$ to break the intermolecular interaction with the nine nearest neighbors for vacancy formation. These energies are estimated to be 9 kJ mol^{-1} for CCl_4 and 5.4 kJ mol^{-1} for $CHCl_3$ for the intermolecular distance of 0.6 nm. In addition, the intermolecular interaction from the second nearest neighbors and the ACF surface atoms will also contribute to the energy for vacancy formation. Taking account of these additional interactions, the estimated values of the energy for vacancy formation are apparently coincident with the activation energy determined from ^{1}H NMR: we conclude that stochastic jumping of the guest molecules between the nearest neighboring sites affects the temperature dependence of the ^{1}H NMR line width, in which the vacancy formation energetically dominates the activation process. For the case of the statistical distribution of CCl_4 and $CHCl_3$, it is expected to increase the activation energy linearly with the population of CCl_4, as shown by dashed line in Figure 6. However, the E_a value suddenly jumps at $f(CHCl_3) = 0.016$. This aspect strongly suggests that molecular self-assembly of CCl_4 takes place in the ACF nanoslit because of the effective intermolecular interaction between CCl_4 molecules. In other words, addition of a trace amount of $CHCl_3$ to CCl_4 molecular assembly destroys the orientational bond order and prevents the formation of an ordered structure.

Such non-ideal behavior of $CHCl_3$–CCl_4 mixture will also hold in the high-concentration region of $CHCl_3$ as well as in the low-concentration region. However unfortunately, the non-ideal behavior at the high concentration of $CHCl_3$ could not be observed in dynamics of $CHCl_3$ molecule, because in that region $CHCl_3$ is the majority component. At high concentration of $CHCl_3$, the non-ideal behavior is expected to be observed in the local structure around a trace of CCl_4, and then the doping effect of CCl_4 to $CHCl_3$ should be monitored by dynamic behavior of CCl_4. Further studies are our next objectives.

Conclusion

Thermal properties were examined using differential thermal analysis of the molecular assembly of CCl_4, $CHCl_3$, and their mixture confined in ACF nanospace with a slit width of 1.1 nm. Results show a hexatic–liquid transition of the CCl_4 molecular assembly in ACF. The transition, however, was not found in mixtures of CCl_4 and $CHCl_3$.

Furthermore, the dynamic features of $CHCl_3$ molecule were investigated using solid-state ^{1}H NMR. The temperature dependence of the ^{1}H NMR line width indicated the local motion of the guest molecules as being much slower than the isotropic reorientational motion. Results also showed that the rate and the activation energy of the local motion depended clearly on the molar fraction of $CHCl_3$ to CCl_4. Doping of a trace amount of $CHCl_3$ to CCl_4 drastically reduced the activation energy for local molecular jumping, implying that the dynamics of guest molecule are also closely related to the phase transition behavior.

The local structure of the guest molecules was discussed in terms of the molecular packing, taking account of the guest–

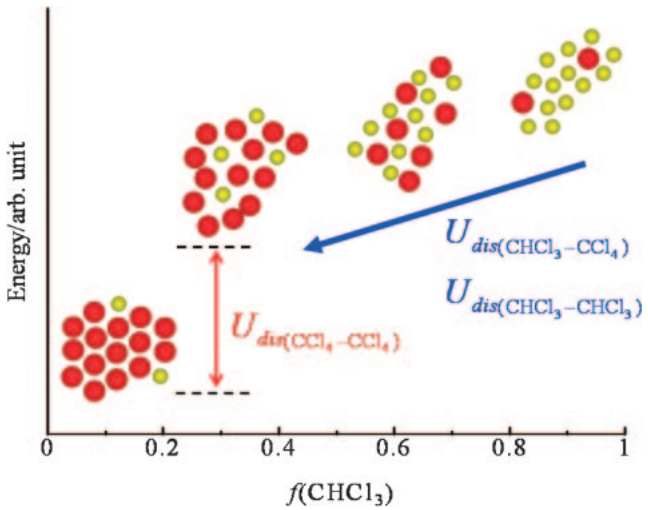

Figure 7. Schematic representation of the local structure for CCl_4 and $CHCl_3$ mixture in ACF. The additivity of the intermolecular interaction among guest molecules will be satisfied at $CHCl_3$ molar fractions of 0.16–1. In this region, $CHCl_3$ and CCl_4 in ACF are mutually solvable. However, at a $CHCl_3$ molar fraction of less than 0.16, the CCl_4 molecules mutually interact and easily become aggregated. Therefore, the effective CCl_4–CCl_4 intermolecular interaction stabilizes the guest molecules, thereby creating the structuralized and ordered molecular arrangement in ACF.

wall potential profile and the relative scale of the guest molecular sizes to the slit space. Saturated amounts of both CCl_4 and $CHCl_3$ suggested the close-packing bilayer structure of the guest molecules into the ACF nanospace. However, the molecular diameter of $CHCl_3$ is somewhat less than the diameter for the ideal close-pack with the bilayer structure in ACF, although CCl_4 has an ideal diameter for close-packing in it. The free space around the $CHCl_3$ molecule can cause the structural fluctuation as well as bring about the high mobility of CCl_4 and $CHCl_3$. This incompatibility between the $CHCl_3$ molecular size and the ACF slit width affects the hexatic–liquid transition behavior.

Finally, we discussed the possibility of the dependence of the activation energy on the molar fraction of $CHCl_3$ based on the intermolecular interaction of the guest molecules. Mainly, three interactions act between $CHCl_3$ molecules and between $CHCl_3$ and CCl_4: electric dipole–dipole, permanent dipole-induced dipole, and dispersion forces. The dispersion force is the dominant interaction among them. In the close-packing bilayer structure of the guest molecules, the dispersion force from the nine nearest neighbors corresponds to the thermal energy for vacancy formation, and reflects the activation energy semiquantitatively for the local molecular jump of the guest molecules. Based on the results in this study, the local structure of the binary mixture of $CHCl_3$ and CCl_4 in ACF is schematically represented in Figure 7. The dependence of activation energy on the molar fraction of $CHCl_3$ indicates that $CHCl_3$ and CCl_4 are solved with each other statistically and homogeneously at molar fractions of $CHCl_3$ of 0.16–1. However, CCl_4 tends to form self-assemblies for molar fractions of $CHCl_3$ of 0–0.16. Especially for doping of a trace amount of $CHCl_3$, molecular self-assembly of CCl_4 might take place in an ACF nanoslit to a remarkable degree because of the effective intermolecular interaction among CCl_4 molecules.

Therefore, we found that the existence of $CHCl_3$ in CCl_4 brings about a remarkable impurity effect on 2D melting and phase transition of CCl_4 confined in ACF nanospace.

This study was supported by Grants-in-Aid for Scientific Research (No. 21350012) from the Japanese Ministry of Education, Culture, Sports, Science and Technology.

References

1 M. Alcoutlabi, G. B. McKenna, *J. Phys.: Condens. Matter* **2005**, *17*, R461, and references are therein.
2 Y. Morioka, J. Kobayashi, I. Higuchi, *J. Colloid Interface Sci.* **1973**, *42*, 156.
3 C. Faivre, D. Bellet, G. Dolino, *Eur. Phys. J. B* **1999**, *7*, 19.
4 C. Alba-Simionesco, B. Coasne, G. Dosseh, G. Dudziak, K. E. Gubbins, R. Radhakrishnan, M. Sliwinska-Bartkowiak, *J. Phys.: Condens. Matter* **2006**, *18*, R15, and references are therein.
5 O. V. Petrov, I. Furó, *Prog. Nucl. Magn. Reson. Spectrosc.* **2009**, *54*, 97.
6 X.-P. Tang, J.-C. Wang, L. W. Cary, A. Kleinhammes, Y. Wu, *J. Am. Chem. Soc.* **2005**, *127*, 9255.
7 Z. Liu, K. Muldrew, R. G. Wan, J. A. W. Elliott, *Phys. Rev. E* **2003**, *67*, 061602.
8 S. Kittaka, S. Ishimaru, M. Kuranishi, T. Matsuda, T. Yamaguchi, *Phys. Chem. Chem. Phys.* **2006**, *8*, 3223.
9 K. Kaneko, A. Watanabe, T. Iiyama, R. Radhakrishan, K. E. Gubbins, *J. Phys. Chem. B* **1999**, *103*, 7061.
10 R. Radhakrishnan, K. E. Gubbins, A. Watanabe, K. Kaneko, *J. Chem. Phys.* **1999**, *111*, 9058.
11 L. Guan, K. Suenaga, Z. Shi, Z. Gu, S. Iijima, *Nano Lett.* **2007**, *7*, 1532.
12 K. Kaneko, C. Ishii, M. Ruike, H. Kuwabara, *Carbon* **1992**, *30*, 1075.
13 M. S. Dresselhaus, A. W. P. Fung, A. M. Rao, S. L. di Vittorio, K. Kuriyama, G. Dresselhaus, M. Endo, *Carbon* **1992**, *30*, 1065.
14 X. Xu, S. A. Rice, *Phys. Rev. E* **2008**, *78*, 011602.
15 M. Li, W. L. Johnson, W. A. Goddard, III, *Phys. Rev. B* **1996**, *54*, 12067.
16 K. Chen, T. Kaplan, M. Mostoller, *Phys. Rev. Lett.* **1995**, *74*, 4019.
17 B. I. Halperin, D. R. Nelson, *Phys. Rev. Lett.* **1978**, *41*, 121.
18 D. R. Nelson, B. I. Halperin, *Phys. Rev. B* **1979**, *19*, 2457.
19 A. P. Young, *Phys. Rev. B* **1979**, *19*, 1855.
20 J. M. Kosterlitz, D. J. Thouless, *J. Phys. Chem. C* **1972**, *5*, L124.
21 R. Radhakrishnan, K. E. Gubbins, M. Sliwinska-Bartkowiak, *Phys. Rev. Lett.* **2002**, *89*, 076101.
22 T. Iiyama, K. Nishikawa, T. Suzuki, T. Otowa, M. Hijiriyama, Y. Nojima, K. Kaneko, *J. Phys. Chem. B* **1997**, *101*, 3037.
23 T. Suzuki, K. Kaneko, K. E. Gubbins, *Langmuir* **1997**, *13*, 2545.
24 T. Suzuki, T. Iiyama, K. E. Gubbins, K. Kaneko, *Langmuir* **1999**, *15*, 5870.
25 T. Iiyama, Y. Kobayashi, K. Kaneko, S. Ozeki, *Colloids Surf., A* **2004**, *241*, 207.

26 T. Ueda, H. Omichi, Y. Chen, H. Kobayashi, O. Kubota, K. Miyakubo, T. Eguchi, *Phys. Chem. Chem. Phys.* **2010**, *12*, 9222.
27 T. Ueda, H. Omi, T. Yukioka, T. Eguchi, *Bull. Chem. Soc. Jpn.* **2006**, *79*, 237.
28 T. T. P. Cheung, *J. Phys. Chem.* **1995**, *99*, 7089.
29 A. Abragam, *The Principles of Nuclear Magnetism*, Clarendon Press, Oxford, **1961**, pp. 451–467.
30 G. W. Smith, *J. Chem. Phys.* **1965**, *42*, 4229.
31 A. Abragam, *The Principles of Nuclear Magnetism*, Clarendon Press, Oxford, **1961**, pp. 111–113.
32 H. Omichi, T. Ueda, Y. Chen, K. Miyakubo, T. Eguchi, *Mol. Cryst. Liq. Cryst.* **2008**, *490*, 91.
33 W. A. Steele, *Surf. Sci.* **1973**, *36*, 317.
34 J. N. Israelachvili, *Intermolecular and Surface Forces*, 2nd ed., Academic Press, London, **1991**, pp. 57–85.